# Numerical Investigation of Cavitation Bubble Dynamics Near Walls

E. Lauer, X.Y. Hu, S. Hickel, and N.A. Adams

## 1 Introduction

The collapse of cavitation bubbles near walls is one of the major reasons for failure of technical devices involving the processing of liquids at large pressure differences. High-speed photography gives a first insight into the bubble dynamics during the collapse [4],[5] and shows two fundamental phenomena during the non-spherical cavitation bubble collapse process: first the development of high-speed jets and second the release of shock-waves upon final bubble collapse. Both, the impact of shock waves and of high-speed jets on a surface can lead to material erosion. A more detailed experimental investigation including a precise determination of peak pressures at the wall and its association with the initial bubble configuration and evolution is beyond current experimental capabilities.

This information can be only obtained from numerical simulations, but the demands on the numerical methods are high. The major challenge for numerical investigations is to accurately reproduce the dynamics of the interface between water and vapor during the entire collapse process including the high-speed dynamics of the late stages, where compressibility of both phases plays a decisive role.

In this paper, we use a model based on the conservative interface-interaction method of Hu et al. [2]. The material interface is accurately resolved by a level-set approach on Cartesian meshes and the interface evolution is computed from a generalized Riemann problem. The effect of condensation and evaporation is taken into account by a non-equilibrium phase-change model.

The objective of this work is to contribute to the clarification of wall-attached cavitation-bubble collapse. Three different configurations of spherical cavitation bubbles are investigated: a detached bubble, a bubble cut by the wall in its lower hemisphere, and one cut by the wall in its upper hemisphere. Depending on the initial wall position, we find a different collapse behavior. We observe wall-normal, as

E. Lauer · X.Y. Hu · S. Hickel · N.A. Adams
Institute of Aerodynamics and Fluid Mechanics, Technische Universität München,
Boltzmannstr. 15, 85748 Garching bei München, Germany

well as wall-parallel jets. In a second step, we focus on the significance of initial bubble asymmetries on the collapse dynamics by considering an initially ellipsoidal vapor bubble attached to a wall. This scenario leads to a significantly different evolution of the topology during the collapse.

## 2 Numerical Approach

Our numerical approach is based on the conservative interface method of Hu et al. [2]. A sharp interface $\Gamma(t)$, which is tracked with the level-set approach of Fedkiw et al. [1], separates vapor ($v$) and liquid ($li$) within the computational domain. We solve the integral form of the Euler equations for both fluids separately on the corresponding subdomains in a conservative way ($m = v, li$).

$$\begin{aligned} V\left(\alpha_m^{n+1}\overline{\mathbf{U}}_m^{n+1} - \alpha_m^n\overline{\mathbf{U}}_m^n\right) = &\int_n^{n+1} dt\ \Delta y\Delta z\left[A_m^{12}(t)\mathbf{F}_m^{12} - A_m^{11}(t)\mathbf{F}_m^{11}\right] \\ &+ \int_n^{n+1} dt\ \Delta x\Delta z\left[A_m^{22}(t)\mathbf{F}_m^{22} - A_m^{21}(t)\mathbf{F}_m^{21}\right] \\ &+ \int_n^{n+1} dt\ \Delta x\Delta y\left[A_m^{32}(t)\mathbf{F}_m^{32} - A_m^{31}(t)\mathbf{F}_m^{31}\right] \\ &+ \int_n^{n+1} dt\ \mathbf{X}_m\left(\Delta\Gamma(t)\right)\ , \end{aligned} \tag{1}$$

where $\alpha_m\overline{\mathbf{U}}_m$ and $\overline{\mathbf{U}}_m$ are the vector of the conserved quantities in the cut cell and the vector of volume averaged conservative variables respectively. $\mathbf{F}_m^{pq}$ is the average flux across a cell face. The volume fractions $\alpha_m$ and the cell-face apertures $A_m^{pq}$ are reconstructed from the level-set field. The coupling between both fluids is achieved by a conservative interface interaction term $\mathbf{X}_m\left(\Delta\Gamma(t)\right)$.

The interaction term accounts for the contributions of pressure force and phase change, respectively,

$$\mathbf{X}_m(\Delta\Gamma) = \mathbf{X}_m^p + \mathbf{X}_m^t\ . \tag{2}$$

From the solution of the two-material Riemann problem at the interface, the interface pressure $p_I$ and the interface normal velocity $\mathbf{u}_I$ serve to compute the pressure term $\mathbf{X}_m^p$

$$\mathbf{X}_m^p = \begin{pmatrix} 0 \\ p_I\Delta\Gamma\ (\mathbf{n}_m\cdot\hat{i}) \\ p_I\Delta\Gamma\ (\mathbf{n}_m\cdot\hat{j}) \\ p_I\Delta\Gamma\ (\mathbf{n}_m\cdot\hat{k}) \\ p_I\Delta\Gamma\ (\mathbf{n}_m\cdot\mathbf{u}_I) \end{pmatrix}\ . \tag{3}$$

The mass transfer term $\mathbf{X}_m^t$ is given by

$$\mathbf{X}_v^t = -\mathbf{X}_{li}^t = \begin{pmatrix} \dot{m}\,\Delta\Gamma \\ \dot{m}\,\Delta\Gamma\,(\mathbf{v}\cdot\hat{i}) \\ \dot{m}\,\Delta\Gamma\,(\mathbf{v}\cdot\hat{j}) \\ \dot{m}\,\Delta\Gamma\,(\mathbf{v}\cdot\hat{k}) \\ \dot{m}\,\Delta\Gamma\left(e_v + \frac{1}{2}|\mathbf{v}|^2\right) + p_I\,\Delta q^*\,\Delta\Gamma \end{pmatrix}, \tag{4}$$

where $\mathbf{v}$ is the velocity of the liquid at the interface in case of evaporation and the velocity of the vapor in case of condensation, respectively. $\Delta q^* = \dot{m}/\rho_{li}$ is the phase-change induced velocity and $\dot{m}$ the phase-change rate obtained from [6]

$$\dot{m} = \frac{\lambda}{\sqrt{2\pi R_v}}\left(\frac{p_s(T_{li})}{\sqrt{T_{li}}} - \frac{p_v}{\sqrt{T_v}}\right). \tag{5}$$

Here, $R_v$ is the specific gas constant in the vapor phase, and $\lambda$ is the accommodation coefficient for evaporation or condensation (assumed to be constant). $T_v$ and $T_{li}$ are the temperatures of vapor and liquid at the phase interface, respectively. $p_v$ is the actual vapor pressure at the interface, and $p_s(T_{li})$ is the equilibrium (saturation) vapor pressure at temperature $T_{li}$.

For our computations, we use a fifth-order WENO scheme [3] and a third-order TV Runge–Kutta scheme [7] to discretize the Euler equations. Simulations are carried out with the CFL number of 0.6. We always model vapor as ideal gas ($p = R\rho T$ with $\gamma = 1.335, R = 461.5\,\mathrm{J/(kg\ K)}$) and use Tait's equation of state for water ($p = B(\rho/\rho_0)^\gamma - B + A$ with $B = 3310\,\mathrm{bar}$, $A = 1\,\mathrm{bar}$, $\rho_0 = 1\,\mathrm{kg/m^3}$ and $\gamma = 7.15$).

## 3 Spherical Vapor-Bubble Collapse

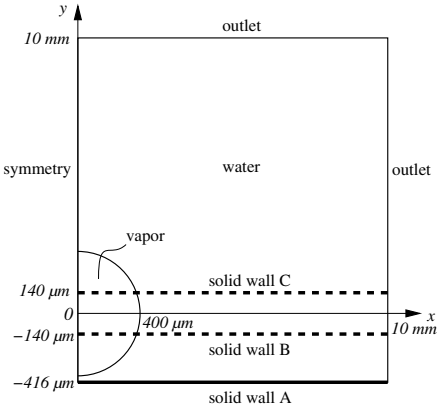


**Fig. 1** Sketch of the problem. Three configurations with different wall positions are investigated.

We investigate the collapse of a vapor bubble near a solid wall. As shown in Fig. 1, the initial bubble radius is 400 µm and we consider three different wall positions A, B and C. We take advantage of symmetries and compute only one quarter of the bubble. The grid spacing is equidistant in the bubble region with 100 computational cells over the initial bubble radius. Grid stretching is applied in the far-field. Outlet boundary conditions are imposed at $x, y, z = 10$ mm. Data are mirrored on the (X-Y)- and (Y-Z)-plane for visualization. Both fluids have a common temperature of 293.0 K which is the saturation temperature corresponding to the initial vapor pressure of 0.0234 bar. Initial liquid pressure is 100 bar and the accommodation coefficient is taken as $\lambda = 0.01$.

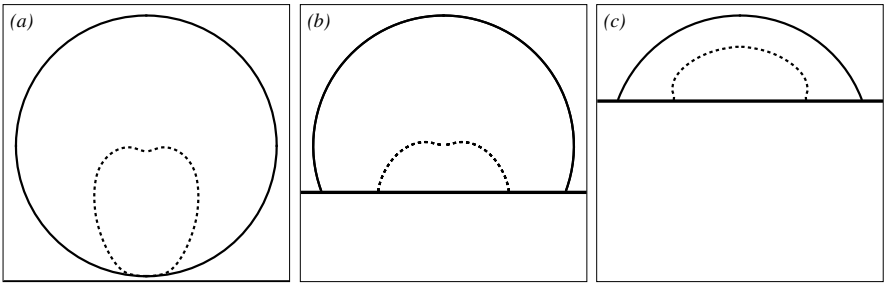


**Fig. 2** Initial situation and bubble shape after cavity development for case A, B and C.

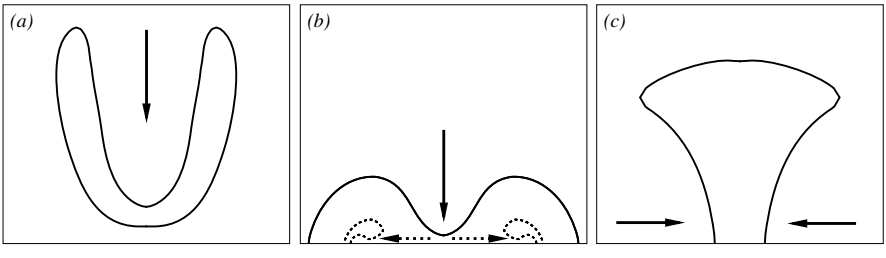


**Fig. 3** Liquid jets during vapor bubble collapse near a wall (frame size in µm): (**a**) Wall-normal re-entrant jet for configuration A (296x244), (**b**) primary wall-normal re-entrant jet (*solid line*) and secondary wall-parallel outward pointing jet (*dashed line*) for configuration B (352x292), and (**c**) wall-parallel inward pointing jet for configuration C (128x104). Arrows indicate the jet direction.

For all configurations, the vapor bubble shrinks slowly during the initial period. The rapid stage of the bubble collapse starts with the development of a cavity, followed by the formation of a liquid jet. Two fundamentally different scenarios at the early stages of bubble collapse can be found. For a detached bubble or a bubble cut in the lower hemisphere, the collapse is initiated at the top of the bubble (Fig. 2 a,b). A fast liquid re-entrant jet develops and penetrates through the bubble

in wall-normal direction (Fig. 3 a,b). For an attached bubble cut in the upper hemisphere, the collapse is initiated between wall and interface (Fig. 2 c) and a liquid jet develops radially towards the bubble center (Fig. 3 c).

The appearance of a secondary jet can be only observed with configuration B since the wall normal re-entrant jet is deflected at the wall and interacts with the remaining bubble ring (Fig. 3 b, dashed lines). This secondary jet is radially symmetric and develops from the symmetry axis outwards in wall-parallel direction. For configuration A no secondary jet develops as the residual bubble ring is not attached to the wall.

Figure 4 gives a three-dimensional visualization of the bubble shape during the stage of the three different liquid jets.

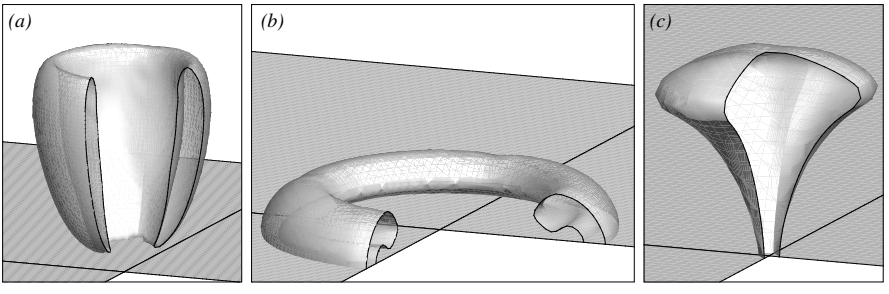


**Fig. 4** Cuts through an iso-surface of the zero level-set (interface) showing the shape of the bubble during the stage of the liquid jets.

The first occurrence of extreme pressure magnitudes coincides with jet breakdown. For cases A and B with a wall-normal re-entrant jet, the observed maximum wall pressures are of comparable magnitude of about 100 times the initial pressure. Slightly larger values for the detached bubble can be attributed to a larger jet velocity. Looking at wall-parallel radial jets, one has to distinguish between the outward-pointing secondary jet of configuration B and the inward pointing primary jet of configuration C. In the latter case, the liquid is gradually compressed while being transported towards the symmetry axis, where maximum pressure occurs. The maximum pressure after inward-pointing, wall-parallel jet breakdown is about six times larger than that for a wall-normal jet. For the outward-running, wall-parallel secondary jet of configuration B, extremely low pressure is observed inside the jet as an expansion of the liquid further decreases the pressure of the high-velocity jet. After the jet breaks down, the liquid pressure increases, but remains significantly smaller than for the inward-pointing jet.

During the final stage of the bubble collapse, two different scenarios occur. For cases A and C, the residual vapor bubble is detached after jet breakdown. Thus, the maximum pressure due to final bubble collapse occurs away from the wall. The emitted shock wave impinges on the wall with reduced magnitude, and the wall pressure does not reach the level observed for jet breakdown. The second scenario

can be found for configuration B. After primary and secondary jet breakdown, a residual vapor ring remains at the wall. This ring is surrounded by high pressure which initiates the final collapse radially towards the symmetry axis. Liquid is compressed towards the center region resulting in large pressure with a maximum at the symmetry axis of about 400 times the initial pressure.

## 4 Ellipsoidal Vapor-Bubble Collapse

The ideal situation of spherical vapor bubbles hardly applies to technical applications, where cavitation bubbles are most likely non-spherical. A moderate increase of geometrical complexity by considering an ellipsoidal vapor bubble near a solid wall allows for an initial estimate on the effect of geometry variations on bubble collapse. As it was found previously that configuration C of a spherical vapor bubble leads to the largest wall pressure, we consider a similar configuration with the ellipsoidal bubble. The equivalent full (non-cut) ellipsoid is rotationally symmetric about the $x$-axis and has the same volume as the spherical bubble of the previous section. We set the length of the semimajor axis to $a = 3/2\, R_{\text{sphere}} = 600\,\mu\text{m}$, where $R_{\text{sphere}} = 400\,\mu\text{m}$ is the initial radius of the corresponding sphere. The volume is kept constant by choosing $b = \sqrt{2/3}\, R_{\text{sphere}} \approx 326.6\,\mu\text{m}$ as the length of the semiminor axis. We use the initial material states given in § 3 and similar grid spacing. Again, only one quarter of the problem is simulated due to sectional symmetry of the setup. For presentation, data are extended to the full domain.

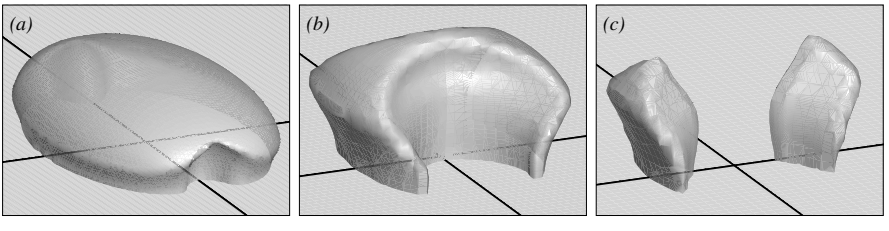


**Fig. 5** Bubble shape during the ellipsoidal-bubble collapse.

For the ellipsoidal bubble the contact angle varies along the circumference. Where the contact angle is small, we expect weak expansion and therefore strong acceleration of the interface. As the contact angle is always below 90° the overall behavior resembles that of configuration C. Along the semimajor axis with smallest contact angle, a jet has already developed in Fig. 5 (a).

Figure 5 (b) shows two different wall-parallel jets. The first jet corresponds to that found already for the spherical bubble. This rotationally symmetric jet leads to a cavity between wall and interface along the circumference of the bubble. The second jet is a consequence of the initial asymmetry. It penetrates into the bubble along the semimajor axis, similarly as a wall-parallel re-entrant jet. It dominates the further bubble collapse as its velocity is larger than that of the first jet.

The axial jet first breaks through the bubble area in the symmetry plane (Fig. 5 c) and two bubble fragments are generated. When the axial jet breaks down, the pressure increases rapidly to more than 100 times the initial pressure. The high pressure between the two bubble fragments initiates the collapse of the residual vapor bubble. The maximum wall pressure is reached at final collapse of the remaining bubble parts. With more than 600 times the initial pressure, the wall pressure is of similar magnitude as for the spherical bubble although the collapse mechanisms are significantly different.

## 5 Conclusions

We have presented simulations with our conservative sharp-interface model for compressible multi-fluid flows with phase-change. Results for the collapse of a spherical vapor bubble close to a solid wall have been discussed for three different bubble–wall configurations. For a detached bubble and a bubble cut by the wall in its lower hemisphere, we found the appearance of the well known wall-normal re-entrant jet. For the latter configuration, also a secondary radial and wall-parallel jet was found. If the bubble is attached, but cut by the wall in its upper hemisphere, the developing jet is wall-parallel and compresses the liquid towards the axis of symmetry. Additional results for the collapse of an ellipsoidal vapor bubble have shown, that the collapse mechanisms is highly dependent on initial asymmetries of the bubble shape.

## References

1. Fedkiw, R., Aslam, T., Merriman, B., Osher, S.: A non-oscillatory Eulerian approach to interfaces in multimaterial flows (the ghost fluid method). J. Comp. Phys. 152, 457–492 (1999)
2. Hu, X.Y., Khoo, B.C., Adams, N.A., Huang, F.L.: A conservative interface method for compressible flows. J. Comp. Phys. 219, 553–578 (2006)
3. Jiang, G.S., Shu, C.W.: Efficient implementation of weighted ENO schemes. J. Comp. Phys. 126, 202–228 (1996)
4. Lindau, O., Lauterborn, W.: Cinematographic observation of the collapse and rebound of a laser-produced cavitation bubble near a wall. J. Fluid Mech. 479, 327–348 (2003)
5. Tomita, Y., Shima, A.: Mechanisms of impulsive pressure generation and damage pit formation by bubble collapse. J. Fluid Mech. 169, 535–564 (1986)
6. Schrage, R.W.: A Theoretical Study of Interphase Mass Transfer. Columbia University Press (1953)
7. Shu, C.W., Osher, S.: Efficient implementation of essentially non-oscillatory shock capturing schemes. J. Comp. Phys. 77, 439–471 (1988)